Post-Print

M. Belan, E. Tescaroli
Discharge Stability Enhancement in Surface Corona Actuators
IEEE Transactions on Plasma Science, Vol. 50, N. 1, 2022, p. 69-78
doi:10.1109/TPS.2021.3132778

Discharge Stability Enhancement in Surface Corona Actuators

Marco Belan and Elia Tescaroli

***Abstract*—A surface corona actuator for flow control, already tested in wind tunnel experiments, is here characterized at the bench in still air. The anodic electrode is provided with periodic triangular tips, and is operated with a pulsed waveform. The operating stability and voltage range turn out to be wider than for DC operation. The actuator is characterized by means of several measurements as function of the frequency, including power absorption and ionic wind measurements in different locations. The ionic wind is measured first by a micropitot probe obtaining time-averaged values, then by a hot wire anemometer obtaining instantaneous velocities and turbulence spectra. The behaviour of the actuator is interpreted accounting for the creation and removal of charges in the gap subject to a periodic excitation.**

***Index Terms*—surface corona discharge, pulsed corona discharge, flow control.**

I. INTRODUCTION

SURFACE plasma actuators are a widely known tool in the fluid-dynamics community to gain control on the behavior of internal and external gas flows by exploiting non-trivial interactions between an ionized gas and the flow to be controlled [1]. The complete lack of moving parts coupled with the inexpensiveness in construction differentiate them from most of the technologies available to date, delivering what can arguably be considered as the most desired characteristics of low weight and high frequency response.

Here the class of surface corona actuators, named after the corona effect they exploit, is considered. First category of EHD devices to be historically conceived, it was rapidly overcome by other varieties primarily because of its uncontrollable tendency to spark formation during operation and high sensitivity to external parameters as humidity and presence of contaminants deposited on the surface, preventing in the past a proper transition from a purely research stage to industrial implementations. Actually, the surface corona discharge is much less controllable than the volumetric corona. A few numerical [2], [3], [4] and experimental [5], [6], [7] studies were devoted to solving these issues, primarily focusing on geometric parameters and materials and almost entirely restricted to the traditional DC power supply.

In the present document a positive pulsed voltage supply is instead appraised, applying a mixed DC+AC waveform to the actuator, and considering its influence on the stability and overall performance parameters compared to previous results obtained with a DC power source. The stability is here quantified in terms of the useful working voltage range, bearing in mind that generally a corona actuator is used at the maximum possible voltage avoiding sparks, in order to create an effective ionic wind. In this sense, high stability also corresponds to low occurrence of transient sparks when operating voltages are at their maximum [8].

It is worth noting that in the huge literature about plasma actuators there is a wide range of alternating and pulsed waveforms applied to the devices, however the vast majority of cases is based on discharges with dielectric barriers, even operated with pulsed DC as in [9], [10], [11], whereas the actuation by corona discharge, with electrodes separated by gas only, is rarely considered [12].

The present experiments are performed at bench in quiescent air, allowing to identify the contribution from the adoption of this power supply and to remove any bias introduced from the presence of an external airflow. A specific multi-tip geometry is considered, already object of previous studies at bench using DC power supply [8], [13], which proved to already partially contribute to the stability improvement of the discharge with respect to a traditional DC wire-plate configuration. Similar geometries with flush-mounted multiple pins were studied also in heat transfer applications [14].

The investigation is carried out by means of mixed electrical, pressure and thermal measurement techniques, focusing on the effects of the periodical excitation and providing insights for further studies on the topic.

II. EXPERIMENT SETUP

A. Electrodes geometry

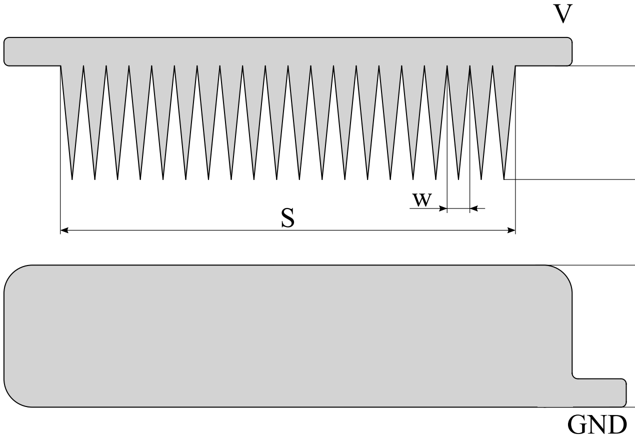

Fig. 1. Bidimensional sketch of a multi-tip actuator: arrangement of the electrodes and outline of the relevant geometrical parameters.

M. Belan is with the Politecnico di Milano, Dipartimento di Scienze e Tecnologie Aerospaziali, via La Masa 34 - 20156 Milano, Italy; e-mail: marco.belan@polimi.it (see http://www.aero.polimi.it/belan).

E. Tescaroli was with the Politecnico di Milano, Dipartimento di Scienze e Tecnologie Aerospaziali.

Manuscript received xxx; revised xxx.

A geometrical sketch representing the class of multi-tip corona actuators considered in the present studies is depicted in Fig. 1. The specific values for the geometrical parameters adopted herein is univocally identified in short by the codename ”C6” as per classification introduced in [13]. This abbreviation identifies an anodic multi-tip electrode consisting of 20 adjacent tips of height $h = 20$ mm and width $w = 4$ mm each, coupled with a rectangular grounded electrode of width $C = 25$ mm and span $S = 100$ mm having rounded corners to avoid undesirable electric field intensifications during operation. Both electrodes are glued on the same side of a flat PMMA surface, maintaining a constant gap $g = 15$ mm between a virtual straight line passing through the vertex of each tip and the front edge of the grounded electrode.

Albeit considerations in the following sections apply to the entire class of multi-tip devices, this particular specimen was selected to allow for comparison of bench results with the ones obtained in wind tunnel tests [15], where this actuator showed remarkable lift and drag enhancement in incipient and deep stall conditions when the same power supply here considered was applied. Here the chosen PMMA dielectric substrate is the same of the wind tunnel version, however further experiments could involve non hygroscopic materials as glass or SiO_2 crystals, capable to influence the actuator performance [5], [16]. The reduced span and number of tips with respect to the wind tunnel model allows to accommodate the device inside the test bench ensuring at the same time to retain a meaningful set of elements to correctly reproduce its behavior. In fact, the creation of periodic electric and motion fields across the actuator span is ensured by the condition $w \ll S$, satisfied both by the wind tunnel actuator and by the present one.

The fabrication of the electrodes involves a sequence of mechanical cutting operations starting from a 0.12 mm thick aluminium adhesive foil tape, preferred over thinner tapes for the greater mechanical robustness and durability offered in previous wind tunnel tests. Since slight differences in the geometry of the tips are possible, an initial examination of the tips was performed via optical microscope inspections to guarantee strict compliance to the nominal geometry. Successive inspections at regular time intervals allowed to monitor the actuator health over operational time by considering the erosion of the tips, which alters their sharpness and the local chemical composition of the conductive material. An excessive increase in the tips curvature radius is in fact a symptom of wear and requires a replacement of the device to ensure conformity to the nominal characteristics. The monitoring process of the geometry over several specimens of the same actuator revealed an average curvature radius of $100 \pm 40\,\mu m$ which was found to be stable over an operating time scale of 100 hours.

B. Electric setup

The actuator is powered by a purposely built power supply, whose electrical scheme is presented in Fig. 2. It includes a sinusoidal input signal generator, an audio amplifier and a high voltage transformer capable of $20kV_{pp}$ at $P = 100$ W. A clamper stage (D_{cl} and C_{cl}=1 nF) is introduced to offset the incoming signal by half of its amplitude, followed by a rectifier diode D_r and a ballast resistor $R_b = 4.4M\Omega$. The 1:1000 voltage divider (R_h and R_l, load 47 MΩ) and the shunt resistor (R_s=68 Ω) are used for the electrical measurements on the actuator, which were acquired by means of a 350 MHz digital oscilloscope with 20 Mrecords/trace. Measurements at the primary winding of the transformer are also possible, thanks to the series resistor R_t. The ideal voltage signal provided to the actuator is sketched in Fig. 2, consisting of a periodic positive waveform of period $T = 1/f$ and amplitude V_{pk}. The real voltage waveform turns out to differ from the ideal one, as discussed in §III, but as the ideal one it periodically crosses the limited range of voltages in which the corona discharge can be sustained, namely between an ignition V_{ign} and a spark V_{spk} thresholds. In particular, the ignition level V_{ign} can be identified by the appearance of a measurable current, larger than 3 σ i.e. 3 times the underlying RMS noise level σ; the spark voltage V_{spk} is clearly marked by the appearance of strong current bursts much larger than the RMS corona current, evidenced by visible and noisy filaments in the discharge. The distance between these limits is influenced by several parameters including the ambient conditions (foremost humidity) and the surface contaminants. Generally, a wider distance ensures an easier setting of the working voltage, usually chosen close to the upper limit to achieve the maximum electric wind intensity.

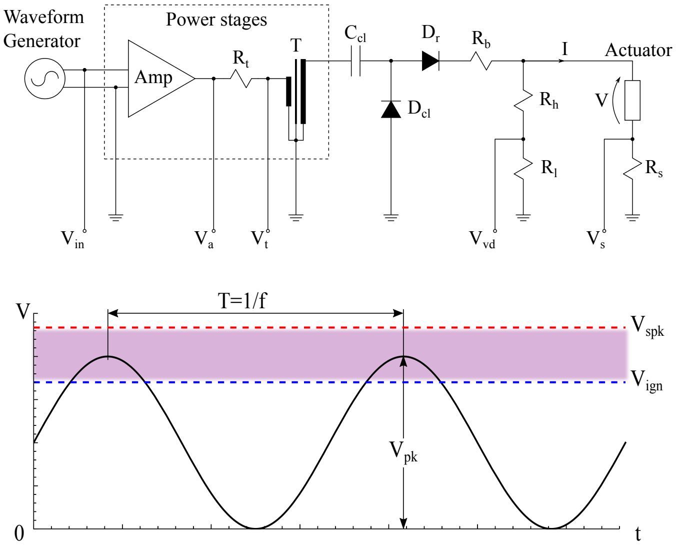

Fig. 2. Scheme of the power supply circuit and devices for electrical measurements (top) and ideal waveform supplied to actuator with range of exploitable voltages for operation defined by the ignition and spark voltages V_{ign} and V_{spk} (bottom).

C. Fluid mechanics measurements

A fluid-mechanic study of the induced flow field was performed involving pressure-based and thermal anemometry to compare performance with previous experiments, including the DC powering tested in [8]. In the test bench, the actuator lies on the floor of a PMMA box of size $0.5 \times 0.3 \times 0.2$ m, as shown in Fig. 3. The box is designed to minimize fluid

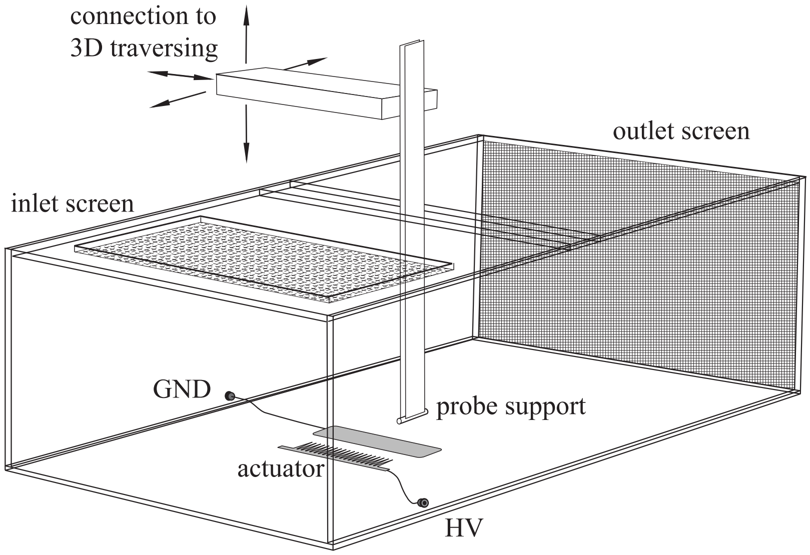

Fig. 3. Drawing of the test bench with mechanical details.

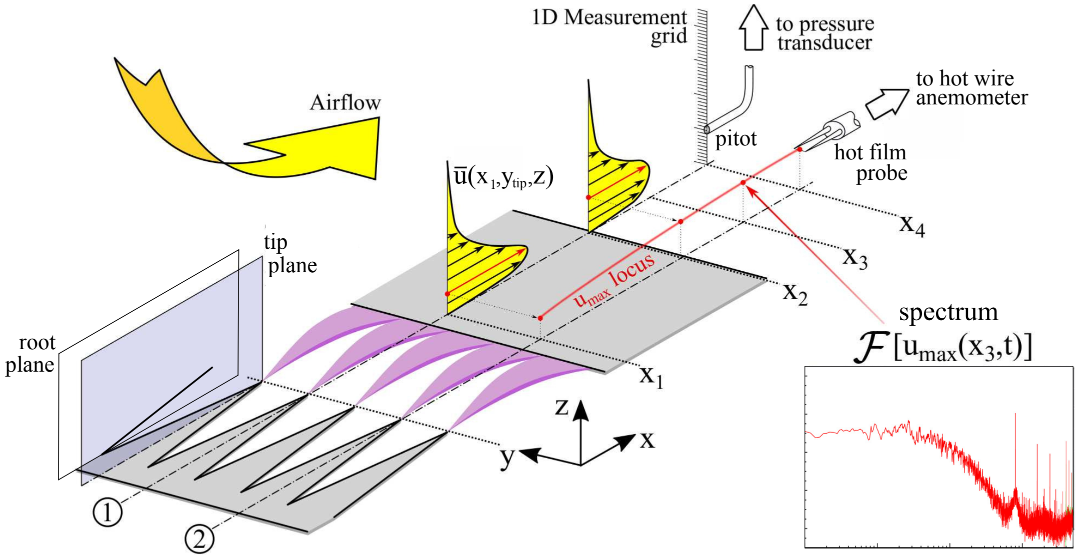

Fig. 4. Perspective view of a spanwise portion of the actuator and operations adopted in the fluid-dynamic characterization. (Phase 1): pressure measurements; (Phase 2): hot wire anemometry. The sketch is for illustration purposes, not to scale.

dynamic disturbances, but it permits the correct development of the induced ionic wind thanks to suitable screens. The screens position accounts for the far field of velocity created by a typical surface actuator, with a slow region upstream of the actuator and a wall jet downstream of it [17], [18]. The screens also allow for proper purging of the box, applying an external suction between tests to avoid excessive ozone concentration. The top is made of mobile sectors, allowing the access to the probes support and the relevant 3D traversing movement.

Fig. 4 illustrates the sequentiality of the tests and the rationale behind it. In Phase 1 of the study, pitot pressure measurements were employed to map the distribution in height (z-direction) of the time-average longitudinal velocity for a progressive departure from the discharge. The span dependence (y-direction) was focused on two positions, namely downstream of the vertices of the tips and of the intermediate or root points. To avoid cluttering in the figure, only alignments of probes with respect to the tips symmetry planes are shown, but the same logic applies to the root planes, centered between tips as shown in figure. Accordingly, the spatial evolution of peak velocity (u_{max} locus) is tracked along the x-direction and the thermal anemometer is then used to investigate the energetic content of the flow in such locations (Phase 2) as the maximum value is assumed to be the entity of interest for flow control purposes. This sequence of operations, as well as the procedure for electrical measurements, was repeated for different input waveform frequencies, as detailed in the following.

Pressure was measured through a Pitot tube made of composite material with inner diameter $d_i = 0.4$ mm and outer-to-inner diameter ratio $\theta = 2$, using a differential pressure transducer (range ± 200 Pa, accuracy 0.05 Pa) and acquiring with a 16-bit acquisition module with a sampling frequency of 10 kHz for a time window of several seconds. The pressures were converted to velocity values according to Bernoulli equation, applying corrections for low Reynolds number, shear and wall proximity effects where due [21]. The thermal sensor is a hot film probe, i.e. a hot wire probe with the wire replaced by a 70 μm diameter quartz cylinder covered by a 0.1 μm nickel film. The active length is 1.25 mm. The overheat ratio $(T_{film} - T_{amb})/T_{amb}$ was set to unity for the entire test campaign to ensure high sensitivity to velocity fluctuations. The probe is controlled by a low noise (2.2 nV/$\sqrt{\text{Hz}}$ equivalent input noise) constant temperature anemometer with fast acquisition, through the same oscilloscope used for electric measurements. Both sensors were rigidly mounted on dedicated supports and positioned via a semi-automated 3-axis traversing system with 5μm position accuracy in each direction, whose correct functionality was preliminarily verified when operating under enabled discharge conditions.

While the Pitot probe had no sort of restriction about its vicinity to the electrodes thank to the entirely dielectric nature of its components, it is worth to mention that conventional thermal anemometry systems, as the one employed in present experiments, involve metallic sensors by own nature (prongs, sensitive element), therefore posing limits on their use in proximity of high electric fields. Indeed, introducing a metallic object inside the electric field generated by the two electrodes may distort both the field and the induced flow, thus invalidating the measurement in the first place. Moreover, the sensor immersed into a high intensity EM field may suffer malfunctioning or - in the worst case - permanent damaging together with the whole anemometer unit in case of sparks propagating towards the sensor and the electric circuits. Although an optically isolated solution for the thermal anemometer circuitry has been proposed in literature [11], a valid alternative could be to identify a spark-free zone behind the grounded electrode where the thermal sensor can be safely used. This was accomplished in preliminary tests by replacing the hot film sensor and upstream circuitry with a dummy probe and equivalent resistive load, respectively, and measuring the current at different stations behind the actuator. Setting the origin $x = 0$ mm at the tips line, from $x = 50$ mm onwards negligible currents flowing through the dummy probe were measured, determining in such a way the frontmost position accessible for thermal measurements. The measuring positions for the two campaigns were then chosen accordingly, i.e. $x_1 = 17$ mm and $x_2 = 40$ mm restricted to Pitot access only with the purpose of characterizing the flow as close as possible to the anode, $x_3 = 50$ mm and $x_4 = 60$ mm accessible to both sensors for complementary measures. Hot film anemometers are also sensitive to the moderate temperature variations induced by the plasma discharge, however the minimum hot wire–anode distance of 50 mm and the high overheat also ensure that thermal effects are weak on the probe, since literature data lead to estimate variations less than 5 K on this distance range [18], [20]. Accurate velocity measurements would still require accounting for these temperature variations, however in this work the hot film signal is only used to determine velocity spectra, and the frequency contents are unaffected by these temperature variations.

III. RESULTS

This section presents the findings of bench tests after the adoption of a pulsed actuation coupled with a multi-tip geometry and outlines the differences with respect to other power supplies and geometries investigated in the past.

The data were collected for a frequency range between 400Hz and 1.5kHz, including the 800 Hz excitation that permits direct comparisons with the results provided in [15] at this frequency, concerning wind tunnel tests on the same actuator applied to a stall control problem.

A. *Impact of a periodical ignition on electrical properties*

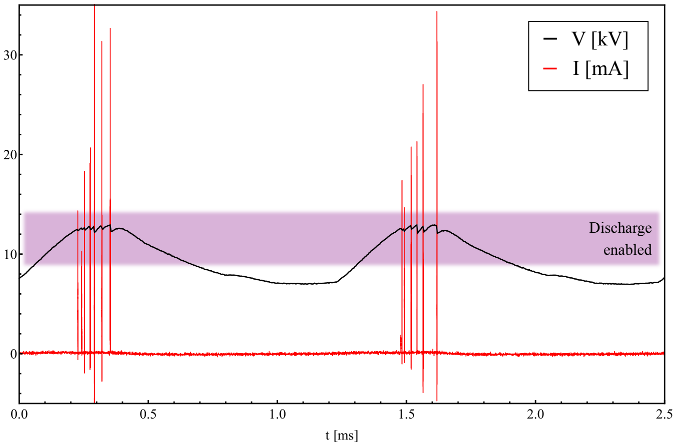

Fig. 5. Sample of the voltage and current signals measured on the actuator for a 800 Hz input excitation with moderate amplitude (the voltage remains well below the spark level).

1) A revised operating principle: As anticipated in §II, the real driving waveform differs from the ideal one. In order to describe how the input waveform affects the operating principle of the actuator, two entire periods of the voltage and current signals measured on the actuator are reported in Fig. 5 for a 800 Hz excitation and a moderate power of 0.76 W, keeping the peak voltage at 12.5 kV$_{pk}$, well below the spark threshold. The corona discharge is periodically activated as desired, but the waveform does not fall to zero between subsequent peaks because of the inherent capacitance of the circuit. When the voltage (black line) falls inside the range identified by the violet band, the plasma discharge is enabled and simultaneous events of ion drift and streamers propagation occur causing the flow of an electrical current (red line) through the gap. Streamers are self-organized ionization waves developing in the gap between the electrodes on a time scale in the microsecond range, with such high current intensity to cause temporary drops in the voltage supply. The strongest intensity streamers develop with the highest voltages and in case of an oscillating input these are accompanied by lower intensity events preceding and following the reach of the top of the oscillation.

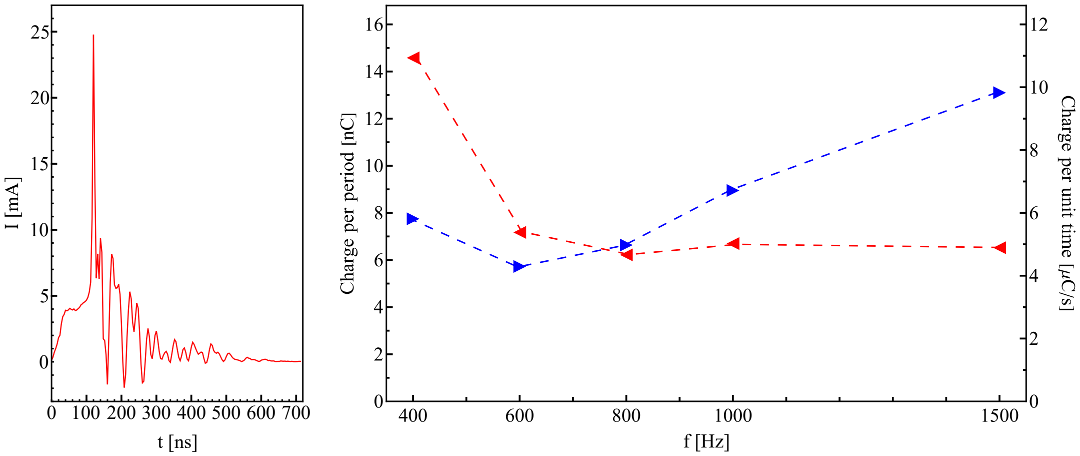

Fig. 6. Streamer current and effects on charge production. Left: average current signal registered during the occurrence of a streamer. Right: average electrical charge injected into the drift region (red: per unit period, blue: per unit time).

During their motion, ions exchange momentum with neutral molecules in the volume above the gap between electrodes causing the development of an ionic wind. According to Moreau [1], both ionic drift and streamer propagation phenomena synergistically contribute to determining the flow control characteristics. Their manipulation can greatly influence the momentum exchange and the stability of the discharge against breakdown occurrence, with the aim of a reliable, uninterrupted operativity.

At a constant voltage level the occurrence of streamers is irregular and influenced by many factors such as the presence of residual charge in the gap. By enforcing a periodical plasma ignition as in Fig. 5, phases of active plasma generation ($V_{ign} < V < V_{spk}$) are being alternated by passive periods ($V < V_{ign}$), each of duration inversely proportional to the frequency of the input signal.

For a given voltage amplitude, the effects of periodical ignition within the examined range ($400 < f < 1500$ Hz) are summarized Fig. 6 and discussed in what follows.

As regards the time scales over which each streamer develops, they appear unaltered by the frequency. Fig. 6 (left) reports an example of the typical current signal during a streamer occurrence, obtained by averaging 25 events: an initial current rise, developing on a 50 ns timescale, precedes the occurrence of a main peak of faster insurgence capable of reaching tens of mA, with the overall process extinguishing in about 500 ns. Streamers may appear either individually or in a series of 2 or 3 subsequent pulses of decreasing peak intensity, but always according to the scales above. The shape and timing found in these experiments are similar with those reported in a recent work from Moreau [22] in which the authors investigated a needle-plate volumetric configuration powered in DC under equivalent discharge conditions.

The number and intensity of the major peaks is instead affected by the frequency in a non-linear fashion. While higher frequencies seem to privilege higher burst intensity, the occurrence per period and their statistical distribution depend on the frequency in a more complicated way. In particular, a statistical analysis performed on the acquired dataset showed that lower excitation frequencies tend to generate more pulses within each period with a low median value and a large scatter on the intensity axis. Increasing the frequency causes the scatter to diminish and the median value to rise. These combined factors cause a partial compensation in the production of charge in each period, as indicated by the red line in Fig. 6 (right), where at 400Hz the charge per period is relatively larger, then for higher frequencies the value stabilizes on a nearly constant level. The plateau in the charge/period curve may favor the higher excitation frequencies as far as ion production is concerned, since more net charge is made available in the drift zone per unit time (blue line).

While the active phases are essential for ions production, the ”off-duty” periods ($V < V_{ign}$) play an important role in the overall functioning of the actuator. The ionic wind velocities reported below in §III-B1 and III-B2 give a Reynolds number between 1000 and 2000, such that when the discharge is off the gas and the residual ions can have inertial motion. The higher frequencies intrinsically involve shorter passive periods, and together with an increased charge per unit time they lead to a lower evacuation of charges from the drift zone. In this compound mechanism, higher frequencies may favor the propagation of streamers of higher intensity and a more efficient momentum exchange with neutral particles because of the higher amount of ions available in the drift zone. However, they may also lead to a higher probability of transition to spark causing a loss of stability.

The above study of the electric properties should be related to the net effect of a periodical ignition as observed in the tests: with respect to a DC excitation, at low frequencies there is a remarkable improvement in stability and a power reduction, whilst for increasing frequencies the stability worsen and the power consumption grows. These two aspects are further discussed in the following of this section. As regards the fluid dynamics effect, the periodical ignition reduces the amount of charge produced compared to a uninterrupted generation in DC, therefore reducing the momentum exchange with neutral particles. This aspect, together with the details on the internal dependency on the frequency, is addressed in §III-B.

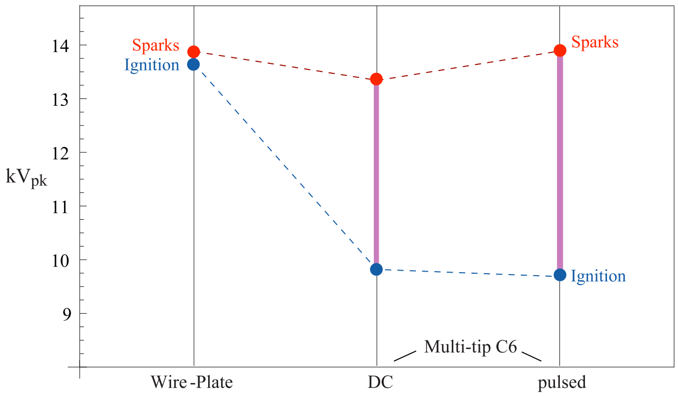

Fig. 7. Outline of the influence of actuator geometry and power supply mode in determining the operating voltage range. The operating conditions are discussed in the body text.

2) Operating voltage range: A quantitative indicator for the stability of a surface corona discharge is represented by the interval between the voltages associated with the occurrence of ignition and spark phenomena, i.e. the operating voltage range $V_{spk} - V_{ign}$. Fig. 7 illustrates the gain in stability according to this parameter considering different geometries and supply combinations on a PMMA surface. The two leftmost columns represent the evolution of such indicator from a traditional DC wire-plate to a DC multi-tip geometry (C6) sharing the same cathode and geometric gap g=15 mm between the electrodes and keeping similar curvature radii for the wire and the tips vertices. In this case, previous works [8], [23] reported a growth from a very narrow 200 V interval to more than 3.5 kV as a consequence of the revised geometry of the anodic electrode. These voltage ranges are also related to the relative humidity RH, that can not overcome 40% for the wire-plate [8], [23] (and the literature [24] reports 50% only admitting non-negligible instabilities), while the range for the multi-tip is measured at its maximum allowed value RH=55%, and is only slightly reduced at RH=40%. Further improvement is achieved with the pulsed actuation applied in the present tests (third column), attaining an ignition-to-spark separation many times larger than the wire-plate and better than for the DC-operated multi-tip. Specifically, the pulsed actuation allows to approach the higher breakdown limit (red markers in Fig. 7) attained by the DC wire-plate ($V_{spk} \approx 13.8$ kV) while maintaining the easier requisite for ignition (blue markers) established by the multi-tip geometry (V_{ign} between 9.7 and 9.9 kV). The voltage range in this case refers to the same RH=55% of the DC case, however with pulsed operation the actuator is capable to operate properly up to RH=63%. Another parameter of relevance for the pulsed case is the frequency: here the reported voltage range holds over the whole considered frequency range, but for $V \approx V_{spk}$ transient sparks become more frequent as f increases, according to the behavior described in the previous subsection.

No remarkable dependence was identified on other thermodynamic variables such as ambient temperature and pressure during the present tests. By tolerating this spectrum of working conditions without degradation of the control performance, the multi-tip geometry actuated with a pulsed supply may lead to a readiness for operation even in some hostile uncontrolled environments found in industrial applications.

3) Electrical power consumption: This is another important performance parameter for plasma actuators. The power is computed as in Eq. (1) by averaging the product of the voltage V and current I signals acquired for a time interval T selected as an integer multiple of the excitation period.

$$W_e = \frac{1}{T}\int_0^T V(t)I(t)\,\mathrm{d}t \tag{1}$$

While the voltage can be safely measured in every condition using the voltage divider shown in Fig. 2 (V_{vd} output), the direct acquisition of the current signal from the actuator (V_s on R_s shunt) is more critical. Indeed, the current signal shown in Fig. 5 was measured at a lower - yet representative - peak voltage compared to the maximum operating value. Even if this actuator has a wide operating range, approaching the upper allowed voltage V_{spk} unavoidably increases the probability to trigger a transient spark, that could bring on the V_s line a dangerous voltage capable of permanently damaging the instrumentation. The alternative method here adopted consists in reading the active power at the primary winding of the transformer by means of the terminals V_a and V_t in the diagram of Fig. 2. Taking into account the efficiency of the transformer, the power available to the secondary winding is obtained, which leads to the calculation of the power absorbed by the actuator and by each component of the secondary circuit. The method has been also validated by comparison with direct measurements at low power levels. Fig. 8 presents the power consumption as function of frequency, setting the actuator at the design operating condition, i.e. close to V_{spk} but avoiding sparks. The crest voltage, determined as average of several peaks in the waveform, is V_{pk}=13.7 kV. The overall trend indicates that power increases with frequency, with higher deviations (1-σ error bars) at higher frequencies due to the worsening in the stability of the discharge, which reflects into greater fluctuations in the absorbed current, as previously mentioned. A comparison with the DC regime can be easily performed by replacing the power stages of Fig. 2 with a

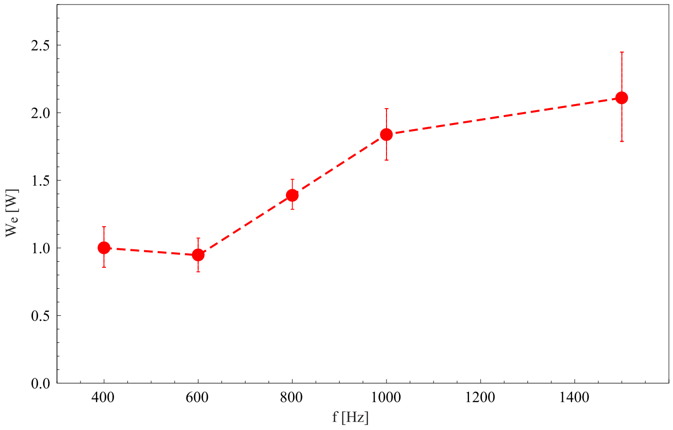

Fig. 8. Electrical power consumption for the Corona C6 actuator driven by a pulsed voltage of variable frequency and constant amplitude (13.7 kV$_{pk}$).

suitable high voltage PSU: setting a V_{DC}=13.3 kV, i.e. at the top voltage without sparks indicated in Fig. 7, it turns out a maximum absorbed power $W_{DC,max}$=2.9 W. The periodic ignition intrinsically implies a reduced active time compared to a continuous operation, causing the power consumption to decrease; in fact, the values in Fig. 8 are all lower than $W_{DC,max}$ even if the stability enhancement from the pulsating supply permits to raise the working voltage with respect to the DC level.

It is worth noting that the power measured at the primary has a different trend, with a minimum around 800Hz already detected in the tests of actuator C6 with wider electrodes in the wind tunnel [15], due to the resonance of the transformer connected to the circuit, a known phenomenon already highlighted in literature [25].

The power absorption of the present actuator can also be compared with the results of previous experiments, accounting for the different conditions and scaling the results on the actuator length. Lowering the DC voltage of the present actuator to V_{DC} =13.0 kV, the measured power/length ratio is 20 W/m, consistent with the 16 W/m measured on a longer version (0.4m) of C6 at the same V_{DC} [13] by observing that in the power/length ratio the end effects are increasingly important on shorter electrodes. Another 0.4m long C6 was tested in pulsed mode with f = 800 Hz on a wind tunnel airfoil [15] and operated at V_{pk}=13.0 kV, with a power consumption of 14.7 W/m. This power is close to the present value in spite of the lower voltage set in wind tunnel tests, however this can be explained by considering that the corona current and power increase when the discharge is subjected to an overlapping gas flow in the same direction, a known phenomenon evidenced both for surface and volumetric corona discharges [26]. In the mentioned wind tunnel tests the airspeed was 20 m/s, i.e. much larger than the ionic wind magnitude.

B. Characterization of the pulsed electric wind

The fluid-mechanical characterization is performed at the scope of identifying the main characteristic of the induced flow: the maximum intensity, the distribution in the lateral direction, the evolution downstream the electrodes and, finally, the frequency content.

1) Average velocity profiles: Relying on the setup described in §II, the study of the induced flow begins with an experimental campaign of total pressure measurements aimed at determining the average velocity distribution $\bar{u}(x_i, y_j, z)$ along the main flow direction ($\hat{x}$) at several stations downstream the anodic electrode (from x_1 to x_4) and for two different span positions, namely on tips and roots planes as shown in Fig. 4. The alignment at y_{tip} and y_{root} is intended to evaluate the periodicity of the field of motion downstream of the actuator.

A sample of average velocity profiles collected for the 800 Hz case is presented in Fig. 9. In the left frame a comparison between tip and root profiles measured at the closest location to the high voltage electrode (x_1 = 17 mm) is presented. The tip profile is clearly more compact, with a higher peak velocity. This is due to the shape of the high-voltage electrode, which creates a discharge consisting of periodic fans starting from the tip vertices [13], also sketched in Fig.4, thus only the tips are sources of momentum in proximity of the actuator surface. The velocity read behind the roots is therefore the result of momentum diffusion in the lateral and vertical directions, which explains the slightly lower peak and more distributed velocity profile in height. The distance between tips is just a fraction of the length scale (thickness) of the wall jet, which is in the order of $\ell \sim 10$ mm: this implies an asymptotic convergence of root and tip velocity profiles for increasing x, finally leading to an almost uniform profile along the span direction. On the other hand, with the present geometry, it can be expected to encounter a larger lateral velocity gradient further upstream.

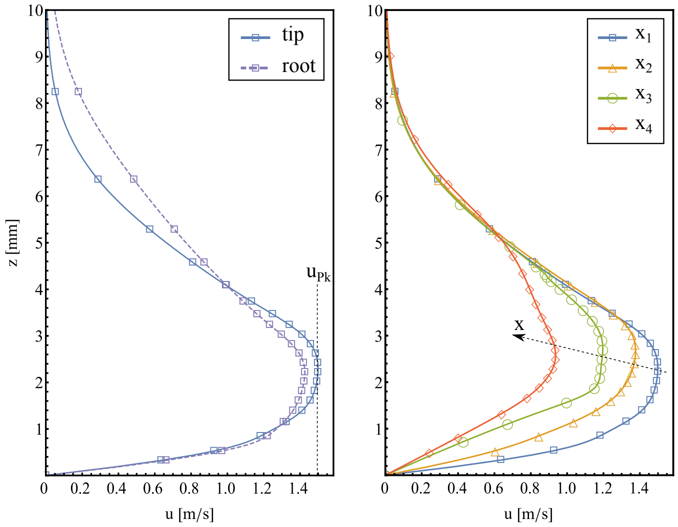

Fig. 9. Average ionic wind velocity profiles from Pitot probe measurements at excitation frequency of 800 Hz. (Left: comparison between tip and root at x_1 = 17 mm. Right: evolution of the tip profile with longitudinal distance.)

Along the tip plane, the curves in the right frame of Fig. 9 illustrate how diffusion operates in the longitudinal direction, together with viscous dissipation at wall, to decelerate and reshape the velocity profiles. Consistently, the flow control strength is higher close to the anodic electrode and aligned with tips.

For the investigated range of frequencies, the maximum velocity grows with the waveform frequency, as indicated by the red points in Fig. 10; the figure includes a simple linear fit but further discussion is provided in what follows. The origin of this behavior can be traced back to the excitation principle discussed in § III-A1: the average amount of charge injected per unit time into the gap increases with the frequency, causing the process of momentum exchange with neutral particles to improve because of the higher amount of ionized particles accelerated by the electric field, hence a greater induced velocity. This statement is supported by the trend found in the measured RMS current flowing through the actuator (blue points in Fig. 10), whose major contribution is indeed provided by the traveling ions. The error bars in Fig. 10, as happens for Fig. 8, are mainly due to the natural fluctuations of the measured quantities, whereas the uncertainty of the measurement system gives only a small contribution. In particular, the velocity fluctuations are studied in detail in the next subsection.

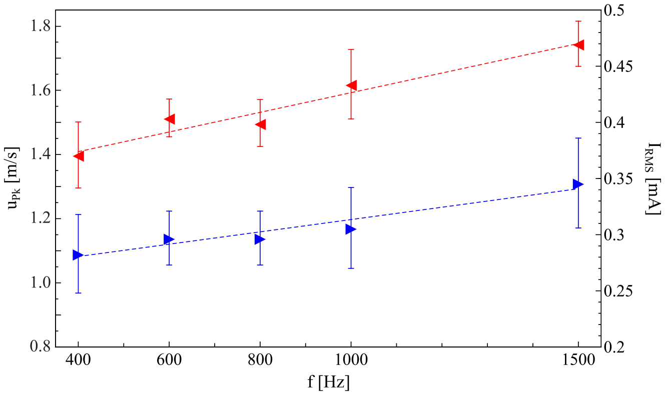

Fig. 10. Trends of peak velocity (red) and RMS current (blue) within the examined frequency range. Data at $x = x_1$ and $V_{pk} = 13.7\,kV$.

The role of the off-duty periods, as done for the stability, has to be discussed for the velocity. Here the 400 Hz frequency is in fact the least performing in terms of induced wind because of the excessive duration of the rest period, which enables a greater amount of ions to escape the drift region and to benefit to a much lesser degree of the compound action previously described in III-A1. Conversely, a frequency increase promotes a better balance between the amount of charge produced and that escaping the gap, increasing momentum and velocity but worsening the stability. This model accounting for the reciprocal roles of active and rest periods is consistent with the results obtained under DC regime [13], [8], since it corresponds to an uninterrupted thrust provided to the fluid, a higher velocity but a worsen stability. In this view the monotonic trend found for the peak velocity in Fig. 10 could be considered as a portion of an exponential law in the form:

$$u_{pk} = A[1 - \mathrm{e}^{\alpha f}] \tag{2}$$

having the asymptotic value $A = 2.5$ m/s set to the DC velocity measured in previous experiments using the same geometry, a value that can be reached when the amount of charge generated per unit time and the loss in momentum between successive cycles become in all respects equivalent to a continuous forcing. In practice, this should happen for pulse frequencies comparable with the natural occurrence of streamers under DC conditions, for this actuator and setup in the order of 10kHz.

To complete the description in the fluid mechanics field, momentum, mechanical power and efficiency achieved by the actuator are briefly discussed. The generated momentum M can be obtained by integrating the momentum flux density ρu^2 across the discharge section (y, z-plane) at a given location x_i, while the mechanical power W_m can be computed by integrating the quantity $\frac{1}{2}\rho u^3$ across the same section, leading to an efficiency parameter $\eta = W_m/W_e$ referred to the electrical consumption W_e treated in §III-A3. For the $f = 800$ Hz case (same frequency of the wind tunnel tests), the comparison with DC values at x_1 gives a momentum $M = 0.32\ M_{DC}$, a power $W_m = 0.18\ W_{m,DC}$ and an efficiency $\eta = 0.25\ \eta_{DC}$. These values improve for increasing f, but remain below DC levels along the considered frequency range, indicating that the pulsed operation does not overcome the steady one in a direct way. The flow control effectiveness evidenced in the wind tunnel tests could therefore be presumably related to the pulsed excitation introduced in the fluid dynamic field. This indicates as further development the measurement of time-resolved velocities in the discharge zone, i.e. in the near field of plasma–gas flow interaction, to determine the instantaneous values of M, W_m and η in this region. However, some insight on the unsteady velocity field can already be obtained by studying the far field by the HWA technique, as shown in the next section.

2) Frequency content of the induced wind: A further step in characterizing the flow can be achieved by means of the hot film probe, thanks to its wide frequency response. In particular, it is possible to verify if any dominant frequency exists in the ionic wind, an information that could improve the comprehension of the phenomena behind the good stall control observed in wind tunnel [15] passing from DC to pulsed actuation under the same geometry. The frequency content is reconstructed by exposing the hot-film sensor to the ionic wind peak $u_{max}(x, t)$, whose height z is known from the previous pitot measurements as visualized in Fig. 4.

As a preliminary procedure, the signal read by the hot-film was carefully examined in order to discern electro-magnetic from fluid-dynamic effects and avoid inferring erroneous properties to the flow. The adopted solution consists of comparing the reading with and without a physical dielectric barrier placed between the actuator and the hot-film. In the former, no convection is cooling the sensor because of the barrier, aside a minimal contribution from natural convection, thus the reading is nearly exclusively generated by ElectroMagnetic Interferences (EMI). In the latter case, forced convection and EMI act simultaneously and cannot be distinguished a priori, but with a simple reference to the previous measurement the EMI can be isolated if sufficiently uncorrelated from the rest of the signal. This is accomplished by comparing the red–green and blue–black lines pairs in Fig. 11, presenting the signal spectra at $x = x_3$ for the $f = 800$ Hz and DC cases, respectively. The curve are spectral power densities normalized with respect to the mean velocity generated by the DC discharge

$$\mathrm{SPD} = 10 \log \frac{|\mathcal{F}[u(t)]|^2}{\bar{u}_{DC}^2}. \tag{3}$$

Considering the pulsed actuation first, with the barrier in place the signal (green line) is mainly due to very narrow peaks concentrated at 800 Hz and multiples (the main peak and the second harmonic are evidenced by green arrows), while the lower end is not populated. Removing the obstacle causes a wide spectrum of low frequencies to appear (red line), corresponding to the partially developed turbulence in the wall jet generated by the actuator, with a Reynolds number Re ranging from 1000 to 1700 for $1.5 < u_{max} < 2.5$ m/s. The turbulence spectrum decreases of -10dB approximately for $f > 100$ Hz, then falls rapidly until, at the 800 Hz driving frequency, the velocity spectrum becomes much lower than the EMI peak. However at this frequency a small wider

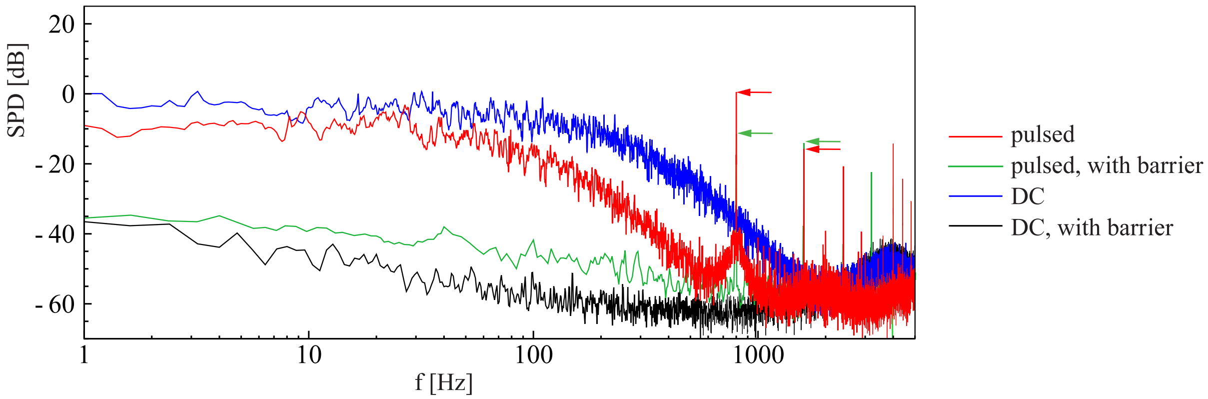

Fig. 11. Spectra of the velocity signal read by the hot film probe at $x = x_3$ for the $f = 800$ Hz and DC cases. Red and green arrows mark the f and $2f$ peaks in the spectra with pulsed actuation.

peak is visible, approximately -35dB high, and appears to be nearly insensitive to the use of different windowing techniques, therefore it could represent a trace of the driving frequency in the velocity field. Finally, at higher frequencies the signal is dominated by the narrow peaks corresponding to harmonics of the main EMI peak, without visible effects on the velocity spectrum. Similar considerations apply to the spectra obtained with different driving frequencies, keeping a constant voltage amplitude: it is easy to see that for increasing driving frequencies, the velocity spectrum extends towards higher f and grows on the dB scale, representing a wall jet of increasing Re. Correspondingly, the EMI peaks appear on the expected values f, $2f$ and higher harmonics.

The DC actuation with the same voltage is also shown in Fig. 11 as a blue line, while the relevant induction on the probe with the barrier in place is the black line. In this case the EMI can not be separated from the global signal since they are due to the irregular induction of the continuous discharge, however the signal with barrier does not contain any specific peak and the whole EMI spectrum lies below -35dB, whereas the velocity spectrum is always consistent with that of a partially developed turbulent flow, with a higher Re than for the pulsed regime.

From Fig. 11 it can be deduced that the ionic wind can fluctuate at the actuation frequency only weakly, when measured at this location downstream the actuator. Nonetheless, a stronger forcing could presumably occurs closer to the ionization region, and in particular inside the gap between the electrodes. Viscosity and diffusion may then cause a progressive weakening of fluctuations for increasing x distances. This is in fact compatible with the findings on a 3D needle-plate case [22] which - as stated in § III-A1 - shares some commonalities with the present surface discharge. Similar properties have been also described for the pulsed ionic wind in DBD actuators [27]. A periodically pulsed velocity in the gap region would also better explain the performance found on a wind tunnel airfoil using the C6 geometry with pulsed actuation: in that case the flow control effect was comparable or better than DC actuation with a lower power absorption. In fact, in that experiment the discharge region was located where flow separation occurs and a periodical forcing might have positively interacted with fluid dynamic structures in the boundary layer of the wind tunnel model.

IV. CONCLUSIONS

The effect of a pulsed power supply applied to a corona actuator presenting a multi-tip anodic electrode has been analyzed in terms of discharge stability enhancement, considering also its impact on performance parameters such as power consumption and induced ionic wind.

The intermittent ignition was shown to cause a remarkable improvement in the stability of the discharge, presumably because of a more balanced injection-disposal of ions from the gap region compared to a classical DC supply. The wide range of operating voltages ensures an easier adjustment of the working point and a lower probability of critical damage events on the device and related equipment.

The coupling of pulsed operation and multi-tip geometry resulted in a more error-tolerant device, capable of withstanding without major penalties minor imperfections in the geometry (for instance related to the fabrication method) and hostile work conditions as humidity and cleanliness of the device. The greater stability enables to reach higher operating voltages with a lower power absorption with respect to a DC supply, however the study revealed that stability worsens when the driving frequency increases. More specifically, the introduction of a pulsed supply improves the stability against transient sparks when the actuator works close to the maximum allowed voltage, but this property requires that the pulse frequency remains low with respect to the natural occurrence frequency of streamers under DC conditions.

The impact on the induced ionic wind intensity has been assessed and related to the electrical properties. With the present geometry the periodic shape of the anode creates multiple parallel wall jets, but the diffusive effects lead rapidly to a nearly uniform velocity field along the span. The time-averaged values of the ionic wind increase with the input waveform frequency, remaining lower with respect to a DC actuation at the same voltage. Correspondingly, also the power absorption grows with the frequency, remaining below the DC power level.

Further measurements of instantaneous velocities have been performed by means of a hot wire anemometer, evidencing the turbulence spectrum of the ionic wind far from the actuator. At the measuring position, the velocity contains only a weak pulsation directly related to the actuation frequency, however this property is important in flow control applications: this point will need further studies aimed at retrieve the instantaneous velocities in the discharge region, in order to comprehend the improved control authority of the present actuator found in wind tunnel experiments.

REFERENCES

[1] E. Moreau, "Airflow control by non-thermal plasma actuators", J. Phys. D: Applied Physics, 40(3), p.605, 2007.

[2] S. H. El-Khabiry, "Numerical evaluation of corona discharge as a means of boundary layer control and drag reduction", Retrospective Theses and Dissertations 10696, Iowa State University, 1994.

[3] S. El-Khabiry & G. M. Colver, "Drag reduction by dc corona discharge along an electrically conductive flat plate for small Reynolds number flow", Phys. Fluids, 9(3), pp.587-599, 1997.

[4] G.M. Colver & S. El-Khabiry, "Modeling of DC corona discharge along an electrically conductive flat plate with gas flow", IEEE Trans. Ind. Appl. 35(2), pp.387-394, 1999.

[5] C. Louste, E. Moreau, G. Touchard, "Influence of an insulating flat plate on a DC surface corona discharge at various air relative humidities", in: Conference Series-Institute of Physics, vol. 178, Institute of Physics, Philadelphia, pp. 273-278, Jan. 2004.

[6] E. Moreau, G. Artana, G. Touchard, "Surface corona discharge along an insulating flat plate in air applied to electrohydrodynamically airflow control: Electrical properties", in: Conference series-Institute of Physics, vol. 178, Institute of Physics, Philadelphia, pp.285-290, Jan. 2004.

[7] A. Labergue, E. Moreau, G. Touchard, "A parametric study of surface corona discharge along an insulating flat plate in atmospheric pressure", in: 2005 Annual Report Conference on Electrical Insulation and Dielectric Phenomena, CEIDP-05, pp. 490-494, Oct. 2005.

[8] F. Messanelli and M. Belan, "Ionic wind measurements on multi-tip plasma actuators," EPJ Web of Conferences 114, 02073, pp. 1–8, 2016.

[9] M.M. Wojewodka, C. White, K. Kontis, "Effect of permittivity and frequency on induced velocity in ac-DBD surface and channel plasma actuators", Sens. Actuators A, 303, 111831, 2020.

[10] Y. Wang, Y. Li, J. Liu, Y. Li, "On the receptivity of surface plasma actuation in high-speed boundary layers", Phys. Fluids, 32 (9), 094102, 2020.

[11] F.O. Thomas, T.C. Corke, A. Duong, S. Midya, K. Yates, "Turbulent drag reduction using pulsed-DC plasma actuation" J. PhyS. D: Applied Physics 52(43), 434001, 2019.

[12] S. Sergeev, H. Lissek, A. Howling, I. Furno, G. Plyushchev, P. Leyland, "Development of a plasma electroacoustic actuator for active noise control applications" J. Phys. D: Appl. Phys., 53 (49), 495202, 2020.

[13] M. Belan and F. Messanelli, "Compared ionic wind measurements on multi-tip corona and DBD plasma actuators," J. Electrostat. Vol. 76, pp. 278–287, 2015.

[14] J. Zhang and F.C. Lai, "Heat transfer enhancement using corona wind generator", J. Electrostat. Vol. 92, pp. 6-13, 2018.

[15] F. Messanelli, E. Frigerio, E. Tescaroli, M. Belan, "Flow separation control by pulsed corona actuators", Exp. Therm. Fluid Sci. 105, pp.123-135, 2019.

[16] J.F. Zhang, D.W. Zhang, X.W. Wu, Q.L. Ren, Z.G. Qu, "Current-voltage characteristics and breakdown of different structural planar microelectrodes in atmospheric air", AIP Advances, 11(6), 2021.

[17] C.-C. Wang, R. Durscher, S. Roy, "Three-dimensional effects of curved plasma actuators in quiescent air", J. Appl. Phys. 109, 083305, 2011.

[18] T.N. Jukes , K. Choi, "Dielectric-barrier-discharge vortex generators: characterisation and optimisation for flow separation control", Exp. Fluids 52: 329-345, 2012.

[19] T.N. Jukes , K. Choi, G.A. Johnson, S.J. Scott, "Characterization of surface plasma-induced wall flows through velocity and temperature measurements", AIAA J. 44, 764-71, 2006.

[20] M. Kotsonis, "Diagnostics for characterisation of plasma actuators", Meas. Sci. Technol. 26, 092001 (30pp), 2015.

[21] C. Tropea, A.L. Yarin, J.F. Foss (Eds.), "Springer handbook of experimental fluid mechanics," Springer Science & Business Media, 2007.

[22] E. Moreau, P. Audier, T. Orriere, N. Benard, "Electrohydrodynamic gas flow in a positive corona discharge", J. Appl. Phys. 125(13), 133303, 2019.

[23] F. Messanelli and M. Belan, "A comparison between corona and DBD plasma actuators for separation control on an airfoil", in: 55th AIAA Aerospace Sciences Meeting, p. 0395, 2017.

[24] L. Leger, E. Moreau, G. Touchard, "Control of low velocity airflow along a flat plate with a DC electrical discharge", in: Conference Record of the 2001 IEEE Industry Applications Conference. 36th IAS Annual Meeting, Vol. 3, pp. 1536-1543, 2001.

[25] J. Kriegseis, A. Duchmann, C. Tropea, S. Grundmann, "On the classification of dielectric barrier discharge plasma actuators: A comprehensive performance evaluation study", J. Appl. Phys. 114(5), 053301, 2013.

[26] L. Zhao and K. Adamiak, "Effects of EHD and External Airflows on Electric Corona Discharge in Point-Plane/Mesh Configurations", IEEE Trans. Ind. Appl. vol. 45, no. 1, pp.16-21, jan./feb. 2009.

[27] M. Forte, J. Jolibois, E. Moreau, G. Touchard, M. Cazalens, "Optimization of a dielectric barrier discharge actuator by stationary and instationary measurements of the induced flow velocity, application to airflow control", In: AIAA Meeting, San Francisco, USA, paper 2006-2863, June 2006.

Marco Belan He received his MSc. (Hons.) in Physics in 1991 from Universitá di Torino and his Ph.D. in Aerospace Engineering in 1995 from Politecnico di Torino. He is currently Associate Professor with the Dipartimento di Scienze e Tecnologie Aerospaziali of Politecnico di Milano, where he has been working since 1999. His research interests include non-equilibrium plasma (plasma-gas flow interactions, ionic propulsion, systems for gas ionization and plasma generation), experimental fluid mechanics (flow control, drag reduction techniques, low pressure and vacuum systems technology, evolution of free hypersonic jets, wind engineering of bluff bodies, design of wind tunnel components). He also works in the field of applied mathematics, dealing with modeling of the laboratory studies above.

Elia Tescaroli He received his MSc. in Aerospace Engineering in 2018 from Politecnico di Milano. Afterwards, Research Assistant with the Dipartimento di Scienze e Tecnologie Aerospaziali of Politecnico di Milano. His research interests include flow control by means of plasma actuators and biomedical applications of plasma to deploy active species against virus and bacteria.